

Model-based asymptotically optimal dispersion measure correction for pulsar timing

K. J. Lee^{1*}, C. G. Bassa^{2,3}, G. H. Janssen², R. Karuppusamy¹,
M. Kramer^{1,3}, K. Liu⁴, D. Perrodin⁵, R. Smits², B. W. Stappers³,
R. van Haasteren⁶, L. Lentati⁷

¹Max-Planck-Institut für Radioastronomie, Auf dem Hügel 69, D-53121 Bonn, Germany

²ASTRON, Postbus 2, 7990 AA, Dwingeloo, The Netherlands

³Jodrell Bank Centre for Astrophysics, University of Manchester, Manchester M13 9PL, UK

⁴Laboratoire de Physique et Chimie de l'Environnement et de l'Espace LPC2E CNRS-Université d'Orléans, F-45071 Orléans Cedex 02, and Station de radioastronomie de Nançay, Observatoire de Paris, CNRS/INSU, F-18330 Nançay, France

⁵INAF-Osservatorio Astronomico di Cagliari, Via della Scienza 5, 09047 Selargius (CA), Italy

⁶Jet Propulsion Laboratory, California Institute of Technology, 4800 Oak Grove Drive, Pasadena, CA 91106, USA

⁷Astrophysics Group, Cavendish Laboratory, JJ Thomson Avenue, Cambridge, CB3 0HE, UK

5 September 2021

ABSTRACT

In order to reach the sensitivity required to detect gravitational waves, pulsar timing array experiments need to mitigate as much noise as possible in timing data. A dominant amount of noise is likely due to variations in the dispersion measure. To correct for such variations, we develop a statistical method inspired by the maximum likelihood estimator and optimal filtering. Our method consists of two major steps. First, the spectral index and amplitude of dispersion measure variations are measured via a time-domain spectral analysis. Second, the linear optimal filter is constructed based on the model parameters found in the first step, and is used to extract the dispersion measure variation waveforms. Compared to current existing methods, this method has better time resolution for the study of short timescale dispersion variations, and generally produces smaller errors in waveform estimations. This method can process irregularly sampled data without any interpolation because of its time-domain nature. Furthermore, it offers the possibility to interpolate or extrapolate the waveform estimation to regions where no data is available. Examples using simulated data sets are included for demonstration.

Key words: pulsar: general — methods: statistical

1 INTRODUCTION

A pulsar timing array is a Galactic-scale experiment, which involves observing an *ensemble of pulsars* and measuring the times of arrival (TOAs) of electromagnetic pulses from these pulsars (see Lommen (2012) for an up-to-date review). Extracting and studying the *common modes* in the TOA data of a pulsar timing array is important for a wide range of astrophysical applications. Three examples of **common modes** are: (i) detecting a gravitational wave background (Jenet et al. 2005), (ii) constructing a pulsar timescale (Hobbs et al. 2012), and (iii) measuring the masses of solar system planets (Champion et al. 2010). Achieving these scientific goals will require the precise measurement of the correlation between the signals emitted by

all of the pulsars of the pulsar timing array. It is therefore critical to reduce the impact of the uncorrelated signals, which represent the ‘noise’ of each individual pulsar.

Timing noise induced by variations in the dispersion measure (DM) is one of the most significant bottlenecks for high precision pulsar timing applications (Armstrong 1984; Foster & Backer 1990; Cordes & Shannon 2010; Jenet et al. 2011). The dispersion results from the speed of electromagnetic waves being frequency-dependent in the dielectric medium. Indeed, dispersion originates from the interaction between the electromagnetic waves and electrons in the interstellar medium. The electromagnetic waves perturb the electrons, which generates a small correction to the arrival times of the original electromagnetic waves. Because of the mass of the electron, the phases of the corrections become frequency dependent (Landau & Lifshitz 1960). In the free electron gas, the difference between the TOA of the electro-

* Email: kjlee@mpifr-bonn.mpg.de

magnetic pulses at two different frequencies (ν_1 and ν_2) is given by:

$$\Delta T = \kappa \frac{\mathcal{D}}{\text{pc} \cdot \text{cm}^{-3}} \left[\left(\frac{\nu_1}{\text{GHz}} \right)^{-2} - \left(\frac{\nu_2}{\text{GHz}} \right)^{-2} \right], \quad (1)$$

if the frequency of the electromagnetic wave is much higher than the plasma frequency, and the magnetic field can be neglected. Here, \mathcal{D} is the DM in unit of $\text{pc} \cdot \text{cm}^{-3}$. The dispersion constant is $\kappa = 4.15 \times 10^{-3} \text{ s}$. The DM is the column density of free electrons, i.e.

$$\mathcal{D} = \int_l n_e dl, \quad (2)$$

where n_e is the electron density, and the integral is performed along the path of wave propagation parameterized by the displacement (l).

Even some of the earliest observations of pulsars, shortly after their discovery, showed clear evidence of DM variations (Rankin & Roberts 1971). DM variations are due to fluctuations in the electron density along the line of sight between Earth and the pulsar. Studying DM variations provides valuable information about the electron density fluctuations and turbulence in the interstellar medium on the scales of 10–1000 AU (Rankin & Counselman 1973; Isaacman & Rankin 1977; Cordes & Stinebring 1984; Cordes et al. 1990; Backer et al. 1993; Phillips & Wolszczan 1991; Kaspi et al. 1994; Wu & Chian 1995; Ramachandran et al. 2006; You et al. 2007; Keith et al. 2013; Petroff et al. 2013). Across a wide spatial frequency range, the electron density fluctuation spectrum usually follows a power law (Armstrong et al. 1995)¹. Recent results by Keith et al. (2013) (i.e. their Fig. 6) had also shown that the structure functions of the DM variations of Parkes Pulsar timing array pulsars are approximately linear in log-log space. Such structure functions imply that the power spectra of the DM variations could be well-approximated by power-law spectra.

This paper builds a model-based algorithm designed to measure DM variations via a unified statistical paradigm, the maximum likelihood estimator (MLE). First, we show in Section 2 that the well-known χ^2 fitting for DM belongs to one of the special cases of MLE. In Section 3, we build the asymptotically optimal (AO) filter to measure the waveform of DM variations, where the MLE for the model parameters is described in Section 3.1 and the MLE for the waveform is presented in Section 3.2. Section 4 contains a demonstration of the method using simulated data sets. In Section 5, discussions and conclusions are presented.

2 ESTIMATING DM FOR A SINGLE-EPOCH OBSERVATION

In this section, we construct the MLEs for the DM and the infinite-frequency TOA. **The high precision infinite-**

¹ The electron density fluctuations are usually described using power-law structure functions rather than a power spectrum (Ishimaru 1978), because the phase correlation function of a scattered wave diverges in a Kolmogorov turbulent medium. The two descriptions are practically equivalent in the context here, where a power-law power spectrum ($\propto q^{-\beta}$) corresponds to a power-law structure function ($\propto r^{\beta-2}$).

frequency TOAs are critical for pulsar timing array projects, while the DM variation measurements are important for investigating the properties of interstellar medium. For a single-epoch observation, we show that this estimator is identical to the standard χ^2 fitting method.

In one observing session, the data are acquired in N_f frequency channels. We denote the center frequency of these channels as ν_k , where $k \in [1 \dots N_f]$. The TOA and its root-mean-square (RMS) error in the k -th channel are T_k and σ_k , respectively. Assuming that the noise in each channel is described by uncorrelated Gaussian random variables, the probability distribution of the TOA is

$$\rho_0(T_k | \mathcal{D}, T_\infty) = \prod_{k=1}^{N_f} \frac{1}{\sqrt{2\pi}\sigma_k} \exp \left[-\frac{(T_k - T_\infty - \kappa \mathcal{D} \nu_k^{-2})^2}{2\sigma_k^2} \right], \quad (3)$$

which is a serial product of individual Gaussian distributions, each of which describes the data for a given channel. T_∞ is the effective TOA measured at $\nu = \infty$. The MLE for \mathcal{D} and T_∞ is constructed to maximize the likelihood, i.e. the value of ρ_0 . This is equivalent to minimizing

$$\chi^2 = \sum_{k=1}^{N_f} \frac{(T_k - T_\infty - \kappa \mathcal{D} \nu_k^{-2})^2}{\sigma_k^2}, \quad (4)$$

which is the well-known χ^2 used for fitting the DM and T_∞ . Therefore, for single-epoch data, the DM χ^2 fitting is the MLE, assuming that the noise in each channel follows an uncorrelated Gaussian distribution.

The MLE (or the χ^2 fitting) can be found analytically by solving $\partial \rho_0 / \partial \mathcal{D} = 0$ and $\partial \rho_0 / \partial T_\infty = 0$, which leads to

$$\widehat{T}_\infty = \frac{\sum_{k=1}^{N_f} \frac{T_k}{\sigma_k^2} \sum_{k=1}^{N_f} \frac{1}{\nu_k^4 \sigma_k^2} - \sum_{k=1}^{N_f} \frac{1}{\sigma_k^2 \nu_k^2} \sum_{k=1}^{N_f} \frac{T_k}{\nu_k^2 \sigma_k^2}}{B}, \quad (5)$$

$$\widehat{\mathcal{D}} = \frac{\sum_{k=1}^{N_f} \frac{1}{\sigma_k^2} \sum_{k=1}^{N_f} \frac{T_k}{\nu_k^2 \sigma_k^2} - \sum_{k=1}^{N_f} \frac{T_k}{\sigma_k^2} \sum_{k=1}^{N_f} \frac{1}{\nu_k^2 \sigma_k^2}}{\kappa B}. \quad (6)$$

Here the symbol $\widehat{\cdot}$ is used to denote the MLEs for the corresponding parameter. Symbol B is defined as

$$B = \sum_{k=1}^{N_f} \frac{1}{\sigma_k^2} \sum_{k=1}^{N_f} \frac{1}{\nu_k^4 \sigma_k^2} - \left(\sum_{k=1}^{N_f} \frac{1}{\sigma_k^2 \nu_k^2} \right)^2 \quad (7)$$

We use the Cramér-Rao bound to estimate the covariance matrix of the MLE, which states that the minimal variances of the MLE are

$$\begin{bmatrix} \langle \delta \mathcal{D}^2 \rangle & \langle \delta \mathcal{D} \delta T_\infty \rangle \\ \langle \delta \mathcal{D} \delta T_\infty \rangle & \langle \delta T_\infty^2 \rangle \end{bmatrix} = \begin{bmatrix} \left\langle \frac{\partial \ln \rho_0}{\partial \mathcal{D}} \frac{\partial \ln \rho_0}{\partial \mathcal{D}} \right\rangle & \left\langle \frac{\partial \ln \rho_0}{\partial \mathcal{D}} \frac{\partial \ln \rho_0}{\partial T_\infty} \right\rangle \\ \left\langle \frac{\partial \ln \rho_0}{\partial \mathcal{D}} \frac{\partial \ln \rho_0}{\partial T_\infty} \right\rangle & \left\langle \frac{\partial \ln \rho_0}{\partial T_\infty} \frac{\partial \ln \rho_0}{\partial T_\infty} \right\rangle \end{bmatrix}^{-1}, \quad (8)$$

where δ denotes the deviation from the expectation, i.e.

$\delta\mathcal{D} = \mathcal{D} - \langle\mathcal{D}\rangle$. From equation (8) we have

$$\langle\delta T_\infty^2\rangle = \frac{1}{B} \sum_{k=1}^{N_f} \frac{1}{\nu_k^4 \sigma_k^2} \quad (9)$$

$$\langle\delta\mathcal{D}^2\rangle = \frac{1}{B\kappa^2} \sum_{k=1}^{N_f} \frac{1}{\sigma_k^2} \quad (10)$$

$$C_{\mathcal{D}, T_\infty} = \frac{\langle\delta\mathcal{D}\delta T_\infty\rangle}{\sqrt{\langle\delta\mathcal{D}^2\rangle\langle\delta T_\infty^2\rangle}} = \frac{\sum_{k=1}^{N_f} \frac{1}{\nu_k^2 \sigma_k^2}}{\sqrt{\sum_{k=1}^{N_f} \frac{1}{\nu_k^4 \sigma_k^2} \sum_{k=1}^{N_f} \frac{1}{\sigma_k^2}}} \quad (11)$$

The estimations for T_∞ and \mathcal{D} are correlated, because the off-diagonal correlation coefficients ($C_{\mathcal{D}, T_\infty}$) are not zero. In order to evaluate the effects of frequency range and TOA measurement accuracy on the estimation of T_∞ and \mathcal{D} , we investigate the special case of $k = 2$, i.e. for dual-frequency data. In this situation, we have

$$\langle\delta T_\infty^2\rangle = \frac{\nu_1^4 \sigma_1^2 + \nu_2^4 \sigma_2^2}{(\nu_1^2 - \nu_2^2)^2}, \quad (12)$$

$$\langle\delta\mathcal{D}^2\rangle = \frac{\nu_1^4 \nu_2^4 (\sigma_1^2 + \sigma_2^2)}{\kappa^2 (\nu_1^2 - \nu_2^2)^2}, \quad (13)$$

$$C_{\mathcal{D}, T_\infty} = \sqrt{\frac{(\nu_1^2 \sigma_1^2 + \nu_2^2 \sigma_2^2)^2}{(\sigma_1^2 + \sigma_2^2)(\nu_1^4 \sigma_1^2 + \nu_2^4 \sigma_2^2)}}. \quad (14)$$

We can investigate the requirements needed to mitigate DM variations in pulsar timing array observations. From equation (12), one can see that the accuracy of infinite-frequency TOA is determined by two major factors: the TOA accuracies of individual bands and the frequency range ($|\nu_1 - \nu_2|$). The figure of merit can be defined as $Q = \nu^4 \sigma$, which evaluates the impact of the particular data sets on the accuracy of the final infinite-frequency TOA. The frequency channel with the largest Q is the dominant source of noise in T_∞ . From the denominator of equation (12), we can also see that the wider the frequency range, i.e. the larger $|\nu_1 - \nu_2|$, the smaller the error in T_∞ . The frequency range has a similar effect on \mathcal{D} , where a larger frequency range gives a smaller error in DM, as well as a smaller correlation between DM and T_∞ .

As shown in Figure 1, for the dual-frequency case, the correlation coefficient $C_{\mathcal{D}, T_\infty}$ depends on the ratio between the two frequencies and the corresponding noise level. The correlation coefficient $C_{\mathcal{D}, T_\infty}$ achieves its maximal value when $\nu_1 = \nu_2$. This is not surprising, since only single frequency data are available, and we thus lose the ability to discriminate between the effects of T_∞ and DM. Figure 1 also suggests that one should further reduce the noise level of the *higher* frequency channel in order to reduce the correlation between DM and T_∞ , while the DM measurement accuracy depends on the noise level of both higher and lower channels as shown in equation (13).

We refer to the above DM estimation method (see also Liu et al. (2013)), which applies to each epoch independently, as the *point-to-point* χ^2 fitting. One can further reduce the statistical error by including the temporal correlation of DM variation in the analysis. Temporal correlations are used in interpolation techniques using polynomials (Kaspi et al. 1994; Freire et al. 2012) and piecewise linear functions (Keith et al. 2013). In the next section, we present the AO algorithm, which also uses temporal correlation information.

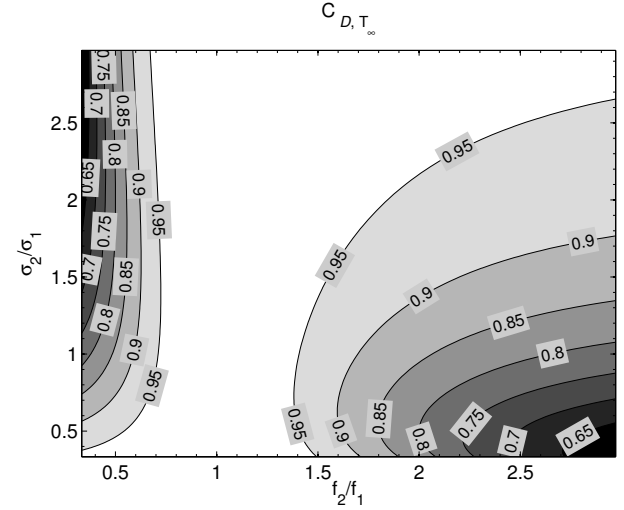


Figure 1. The correlation coefficient $C_{\mathcal{D}, T_\infty}$ between the estimation of DM and T_∞ as a function of frequency and noise level ratios. The x-axis represents the ratio between the two frequencies, while the y-axis represents the ratio between the noise levels of corresponding channels. The correlation coefficient achieves its maximal value of 1 when $\nu_1 = \nu_2$. As indicated in the figure, the parts of parameter spaces that show relatively low correlation values are in the upper-left and lower-right corners. The noise level of the *higher* frequency channel therefore needs to be reduced in order to resolve the correlation between DM and T_∞ .

3 THE AO ESTIMATOR FOR DM VARIATION AT MULTIPLE EPOCHS

In this paper, the term ‘AO’ is used in a strictly statistical sense, i.e. only to describe the statistical properties of the estimator, where the variance of the estimator achieves the Cram r-Rao bound when the signal-to-noise ratio becomes large (Dodge 2006). The AO algorithm is a model-based method, where power-law spectra with unknown amplitudes and spectral indices are assumed for red noise and DM variations. The AO algorithm contains two major steps, 1) estimating the model parameters (in Section 3.1) and 2) constructing the optimal filter to recover the waveform (in Section 3.2).

3.1 MLE for model parameters

In order to use the information encoded in the temporal correlations, we need the corresponding statistical model. We assume that the pulsar TOA contains: 1) the TOA at infinite frequency specified by the timing model (T_∞), 2) DM-variation induced noise ($t_{\mathcal{D}}$), 3) red-noise components independent of observing frequency (r), 4) instrumental delay for the particular equipment (t_s), and 5) radiometer and jitter noise (n). The statistical properties that we assume for each of the components are described below.

- The TOA at infinite frequency (T_∞) is a *deterministic* signal specified by the timing model, i.e. it can be calculated from the timing parameters λ , e.g. pulsar period, period derivative, binary parameters etc. (see Edwards et al. 2006 for details). Although the timing model makes T_∞ nonlinearly dependent on the timing model parameters λ , we

can linearize the model around a given set of timing parameters (van Haasteren et al. 2009). Usually, we can choose the pre-fit timing parameters as the reference point for this linearization, which gives

$$T_{\infty,i} = T_{\infty,0,i} + \sum_k D_{ik} \lambda_k, \quad (15)$$

where i is the index of the TOA data, and k is the index of the timing parameters. The $T_{\infty,0,i}$ are the TOAs specified by the pre-fit timing parameters, D_{ik} is the design matrix². Note that the data point index i is merely a label for the TOA.

- The signal induced by DM variations ($t_{\mathcal{D}}$) is a *frequency-dependent stochastic signal*. It is determined by the DM value at each epoch, as well as the center frequency as shown in equation (1). There usually are time offsets between the TOA data from different instruments or telescopes. These offsets **together with the intrinsic pulse profile evolutions**, without calibration, spoil the measurements of the absolute DM. On the other hand, the variation of DM introduces time-dependent differential delays between frequency channels. It is thus possible to determine the DM variation from the TOA data with arbitrary time-constant offsets between different instruments. The DM variance induced signal is

$$t_{\mathcal{D},i} = \kappa \delta \mathcal{D}_i \nu_i^{-2}. \quad (16)$$

We model the DM variation as a Gaussian stochastic signal with a power-law spectrum, i.e. the DM variance spectrum $S_{\delta \mathcal{D}}$ is defined as

$$S_{\delta \mathcal{D}}(f) = \frac{A_{\mathcal{D}}^2}{f} \left(\frac{f}{f_c} \right)^{-2\alpha_{\mathcal{D}}}. \quad (17)$$

Without loss of generality in the rest of the paper, we use the characteristic frequency $f_c = 1 \text{ yr}^{-1}$. Note that f is the frequency of the signal in the TOAs, which is very different from ν_i , the observing center radio frequency for the i -th data point. The Fourier transform of the spectrum gives the temporal correlation of $t_{\mathcal{D}}$ such that

$$\langle t_{\mathcal{D},i} \rangle = 0, \quad (18)$$

$$C_{\mathcal{D},ij} = \langle t_{\mathcal{D},i} t_{\mathcal{D},j} \rangle = \frac{\kappa^2 \int_{f_L}^{\infty} S_{\delta \mathcal{D}}(f) \cos(2\pi f t_{ij}) df}{\nu_i^2 \nu_j^2}, \quad (19)$$

where t_{ij} is the time lag between the i -th and j -th data point. Lee et al. (2012) and van Haasteren & Levin (2013) have shown that removing a constant value from the power-law noise is sufficient for regularizing the signal, if $\alpha_{\mathcal{D}} < 1$ (i.e. the power spectral index < 3). This gives $f_L \simeq 1/T$, where T is the total time span of the available data. However, for general cases with a steeper spectrum, we need to include f_L as one of the model parameters, otherwise $C_{\mathcal{D}}$ diverges.

In order to see how we can measure the low frequency cut-off from data of a shorter length, we plot the time domain correlation functions of general red noise with different sets

² Although the timing software usually iterates the fitting procedure, the linearity is a valid approximation for the current application, where the TOA differences between the full timing model and the linearized model are smaller than the signals under investigation.

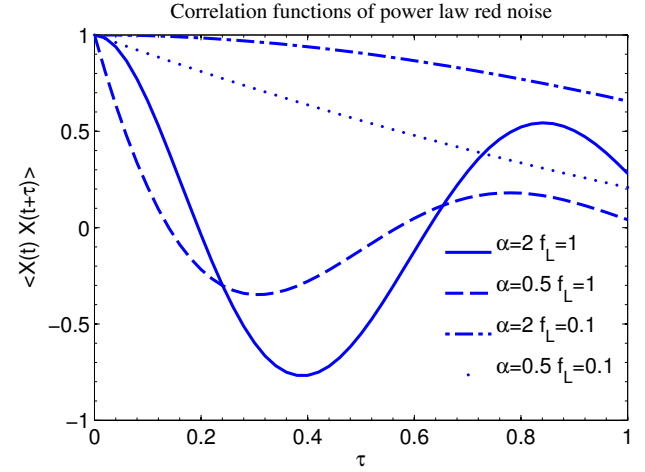


Figure 2. The correlation function of power-law red noise normalized by its autocorrelation. The time τ takes units of data length T , while f_L takes units of $1/T$. The power indices and low frequency cut-offs are given in the legend, where α is the spectral index of the characteristic amplitudes as used in this paper.

of f_L and spectral index α values in Figure 2. Since the shape of the correlation function is sensitive to both the power index and the low frequency cut-off, the values of the two parameters can be inferred.

- Extra time-dependent delays (t_s) could be introduced in the TOAs due to instrumental effects. For example, changing the cable length or switching backends would introduce sharp features in the TOA data. We assume that such an instrumental delay has been calibrated or fitted via the timing parameters (e.g. the ‘jump’ parameter). In these cases, the instrumental delay is either modeled or included in the design matrix D_{ik} , and therefore we do not discuss t_s further in this paper.

- The red-noise component (r) is used to describe the intrinsic timing noise of the pulsar or other frequency independent signals, e.g., a signal induced by the gravitational-wave background, clock noise, or long-term stochastic systematics. We model this component as power-law spectral Gaussian noise in the same way we modeled DM variations. The spectrum and correlation of r are similar, such that

$$S_r(f) = \frac{A_r^2}{f} \left(\frac{f}{f_c} \right)^{-2\alpha_r}, \quad (20)$$

$$\langle r_i \rangle = 0, \quad (21)$$

$$C_{r,ij} = \langle r_i r_j \rangle = \int_{1/T}^{\infty} S_r(f) \cos(2\pi f t_{ij}) df. \quad (22)$$

Because of the fitting of the pulse period and its derivative, red noise signals with $\alpha_r < 5$ are regularized (Lee et al. 2012). We use $1/T$ as the low frequency cut-off.

- The white noise (n) comes from two main different sources: the radiometer noise, which is due to the finite radio flux, and the jitter noise due to pulse jitter (Liu et al. 2012; Cordes & Shannon 2010). There are other possible sources of white noise (Cordes & Shannon 2010). In this paper, we assume that the RMS levels of the radiometer noise are the TOA uncertainties multiplied by a coefficient called ‘Efac’, where TOA uncertainties are determined using standard pulsar timing software (Hotan et al. 2004). Because jitter

noise is uncorrelated with radiometer noise, the correlations of the white noise components are

$$\langle n_i \rangle = 0, \quad (23)$$

$$C_{n,ij} = \langle n_i n_j \rangle = \delta_{ij} (\text{Ef}ac^2 \sigma_i^2 + \sigma_J^2), \quad (24)$$

where σ_i is the error bar of the i -th data point, and the Kronecker $\delta_{ij} = 1|_{i=j}$, otherwise $\delta_{ij} = 0$. σ_J is the RMS of the jitter noise. The definition we use is slightly different from the Tempo2 convention, which uses another parameter ‘Equad’ instead of σ_J , such that

$$C_{n,ij} = \delta_{ij} \text{Ef}ac^2 (\sigma_i^2 + \text{Equad}^2). \quad (25)$$

With the statistical specification of the signal components given above, the joint probability distribution of all TOAs T_i is

$$\rho_0(T_i | \lambda_k; A_{\mathcal{D}}, \alpha_{\mathcal{D}}; A_r, \alpha_r; \sigma_J) = \frac{\exp \left[-\frac{X^2}{2} \right]}{\sqrt{(2\pi)^{N_{\text{pt}}} |C_{ij}|}}, \quad (26)$$

where N_{pt} is the number of data points and $|C_{ij}|$ is the determinant of the correlation matrix $C_{ij} = \langle (T_i - \langle T_i \rangle)(T_j - \langle T_j \rangle) \rangle$. The C_{ij} can be calculated from equation (19), (22), and (24) as

$$C_{ij} = C_{\mathcal{D},ij} + C_{r,ij} + C_{n,ij}. \quad (27)$$

X^2 is the *generalized* χ^2 defined as

$$X^2 = \sum_{i,j=1}^{N_{\text{pt}}} (T_i - T_{0,i} - \sum_k D_{ik} \lambda_k) C_{ij}^{-1} (T_j - T_{0,j} - \sum_{k'} D_{jk'} \lambda_{k'}), \quad (28)$$

where C_{ij}^{-1} is the inverse of C_{ij} , i.e. $\sum_{l=1}^{N_{\text{pt}}} C_{il}^{-1} C_{lj} = \delta_{ij}$. Since $T_i - T_{0,i}$ are the pre-fit timing residuals R_i , equation (28) can be re-written using pre-fit timing residuals as

$$\chi^2 = \sum_{i,j=1}^{N_{\text{pt}}} (R_i - \sum_k D_{ik} \lambda_k) C_{ij}^{-1} (R_j - \sum_{k'} D_{jk'} \lambda_{k'}). \quad (29)$$

The MLE is used to find the parameters $A_{\mathcal{D}}, \alpha_{\mathcal{D}}, A_r, \alpha_r$, Efac, and σ_J in order to maximize the value of likelihood (i.e. distribution function ρ_0). This is similar to the generalized least squares (GLS) methods (Coles et al. 2011)³. The major difference between the two methods is that the GLS assumes the correlation matrix to be known, while the MLE does not. They become identical if the noise model parameters are known as prior information. The two methods are asymptotically identical given that the noise model parameters used in the GLS were estimated by the method asymptotically identical to the MLE. To the authors’ knowledge, there is no work yet that addresses the asymptotic behavior of GLS estimators (Coles et al. 2011) used in pulsar timing applications.

Focusing on the noise model parameters, we find that the linearized pulsar timing parameters (λ_k) can be marginalized analytically (van Haasteren et al. 2009), i.e. we define the reduced likelihood as

$$\begin{aligned} & \rho(R_i | A_{\mathcal{D}}, \alpha_{\mathcal{D}}; A_r, \alpha_r; \sigma_J) \\ &= \int \rho_0(R_i | \lambda_k; A_{\mathcal{D}}, \alpha_{\mathcal{D}}; A_r, \alpha_r; \sigma_J) \prod_k d\lambda_k, \end{aligned} \quad (30)$$

³ Although Coles et al. (2011) use the term ‘Cholesky method’, we prefer to use ‘generalized least squares’ which is widely used in the statistical literature (Kariya & Kuruta 2004).

and one can show that

$$\rho = \sqrt{\frac{|C'_{kk'}|(2\pi)^M}{|C_{ij}|(2\pi)^{N_{\text{pt}}}}} \exp \left[\frac{-X'^2}{2} \right], \quad (31)$$

where

$$C'_{kk'} = D_{ik} D_{jk'} C_{ij}^{-1}, \quad (32)$$

and

$$X'^2 = \sum_{i,j,l;k,k'} R_i (C_{ij}^{-1} - C_{il}^{-1} D_{lk} C'_{kk'}^{-1} D_{l'k'} C_{l'j}^{-1}) R_j. \quad (33)$$

In this way, the parameter estimation problem after marginalizing the pulsar timing parameters is still Gaussian. The noise model parameters and their errors can now be inferred using the Markov chain Monte Carlo (MCMC) method as described in many standard references (Press et al. 2007). We present examples in Section 4.

3.2 Waveform estimator given the noise parameters

With the noise model parameters inferred using the MLE described in the previous section, we are able to construct the MLE for the waveform of each signal component. We note that the identical filter has been derived independently many times in several different areas of research (Lee 1967; Enßlin & Frommert 2011; Deng et al. 2012). We therefore describe the filter only briefly in this paper.

The joint probability distribution, as a function of the individual waveforms, is

$$\begin{aligned} & \rho(r_i, n_i, t_{\mathcal{D},i} | A_r, \alpha_r, \sigma_J, A_{\mathcal{D}}, \alpha_{\mathcal{D}}) = \\ & \mathcal{G}(t_{\mathcal{D},i}, C_{\mathcal{D},ij} | A_r, \alpha_r) \mathcal{G}(r_i, C_{r,ij} | A_r, \alpha_r) \mathcal{G}(n_i, C_{n,ij}), \end{aligned} \quad (34)$$

where the function $\mathcal{G}(x_i, C_{ij})$ is the multi-dimensional zero-mean Gaussian distribution for the vector x_i , of which the covariance matrix is C_{ij} . Signals r_i, n_i , and $t_{\mathcal{D},i}$ are constrained such that their summation is equal to the timing residual, i.e.

$$R_i = r_i + n_i + t_{\mathcal{D},i}. \quad (35)$$

The maximum likelihood waveform estimator (MLWE) is found by maximizing equation (34) under the constraint given by equation (35). This can be done by calculating the variation of ρ with respect to the waveform r, n , and $t_{\mathcal{D}}$. These MLEs are

$$\hat{r}_i = C_{r,ij} C_{jl}^{-1} R_l, \quad (36)$$

$$\hat{t}_{\mathcal{D},i} = C_{\mathcal{D},ij} C_{jl}^{-1} R_l, \quad (37)$$

$$\hat{n}_i = C_{n,ij} C_{jl}^{-1} R_l. \quad (38)$$

$$\hat{R}_{\infty,i} = C_{\infty ik} C_{kj}^{-1} R_j, \quad (39)$$

where the $\hat{R}_{\infty,j}$ are the estimated effective timing residuals, which one would measure at infinite frequency. $C_{\infty ik}$ is defined as

$$C_{\infty ik} = C_{r,ik} + C_{n,ik}. \quad (40)$$

We plot the optimal filter (i.e. a single row of the filter matrix $C_{\mathcal{D},ij} C_{jl}^{-1}$) for the DM variation signal in Figure 3. The spread of the filter around $\tau = 0$ shows the optimal weights used to combine nearby data points for the estimation of DM variations. In the point-to-point fitting method,

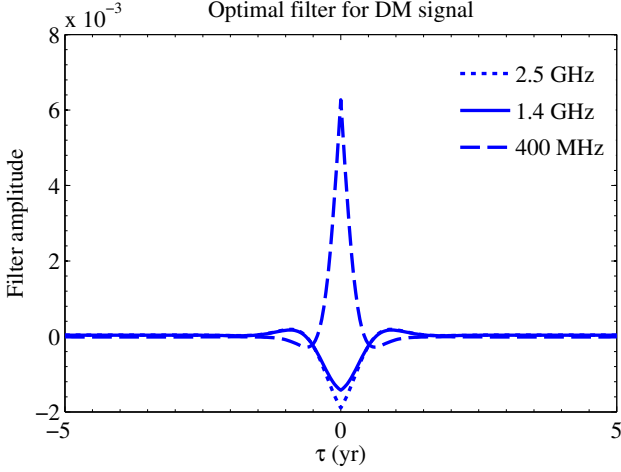


Figure 3. An example of the optimal filter used to reconstruct DM variations. The x-axis represents the time lag, while the y-axis represents the amplitude of the filter. The data set contains three frequencies (400 MHz, 1.4 GHz, and 2.5 GHz), resulting in three curves in the figure, which together form the optimal filter. The maximum of the filter at zero-time lag shows that most of the information needed to estimate DM comes from nearby data points, while the width of the filter shows the weights used for combining data sets. This is different from the point-to-point fitting algorithm, a delta function on this plot, in which no other data points are used to estimate DM variation at any given epoch. Note that we only plot a single row of the filter matrix here. This corresponds to a filter at a single epoch. The filters are calculated for $A_r = 20$ ns, $A_{DM} = 2 \times 10^{-6}$ pc cm $^{-3}$, $\alpha_r = -1.67$, and $\alpha_{DM} = -1.5$.

one ‘subtracts’ the higher frequency residuals from the lower frequency residuals in order to estimate the DM. In this way, the filter functions take negative values at higher frequencies. This naturally arises when constructing the optimal filter.

Usually, the standard deviation of the estimator is used as the error bar on the waveform estimator. However, here the ‘noise’ components are *correlated*, i.e. $\langle (\hat{R}_{\infty,i} - \langle \hat{R}_{\infty,i} \rangle) (\hat{R}_{\infty,j} - \langle \hat{R}_{\infty,j} \rangle) \rangle \neq 0$, because of the red-noise components (r_i). This makes the error bar-type interpretation for the RMS value meaningless, since the error bar is defined such that the noise is uncorrelated. However, for practical purposes, we suggest using the covariance matrix to quantify the waveform uncertainties, where the diagonal terms of the covariance matrix are the $1\text{-}\sigma$ error bars of the estimator. Taking the red noise component as an example, the covariance matrix of the estimated waveform deviations from the true value is

$$\epsilon_{r,ij} = \langle (\hat{r}_i - r_i)(\hat{r}_j - r_j) \rangle. \quad (41)$$

One can show that (Appendix A)

$$\epsilon_{r,il} \simeq C_{r,il} - C_{r,ij} C_{jk}^{-1} C_{r,kl}. \quad (42)$$

Table 1. Parameters used in the examples

Case	A_r (ns)	α_r	A_{DM} (pc cm $^{-3}$)	α_{DM}	$f_{L,DM}$ (Hz)
1	5.0	-1.67	2×10^{-6}	-1.5	3.17×10^{-9}
2	5.0	-1.67	2×10^{-7}	-1.5	3.17×10^{-9}
3	2.0	-1.67	5×10^{-8}	-1.5	3.17×10^{-9}
4	5.0	-1.67	2×10^{-7}	-1.5	6.34×10^{-10}
5	5.0	-1.67	N/A	N/A	N/A

The data length in all cases is 10 years with an average cadence of 1.5 month. In all simulations, we have used $E_{fac} = 0$ and $f_{L,red} = 1/T$. The white noise RMS levels are 100 ns for all frequencies and cases. In case 5, a square-waveform DM variation is simulated, with a duration of 1 year and an amplitude of 2×10^{-5} pc cm $^{-3}$.

Similarly the covariance of other waveform estimators are

$$\begin{aligned} \epsilon_{\mathcal{D},il} &= \langle (\widehat{t_{\mathcal{D}i}} - t_{\mathcal{D}i})(\widehat{t_{\mathcal{D}j}} - t_{\mathcal{D}j}) \rangle \\ &\simeq C_{\mathcal{D},il} - C_{\mathcal{D},ij} C_{jk}^{-1} C_{\mathcal{D},kl}, \end{aligned} \quad (43)$$

$$\begin{aligned} \epsilon_{n,il} &= \langle (\widehat{t_{ni}} - t_{ni})(\widehat{t_{nj}} - t_{nj}) \rangle \\ &\simeq C_{n,il} - C_{n,ij} C_{jk}^{-1} C_{n,kl}, \end{aligned} \quad (44)$$

$$\begin{aligned} \epsilon_{R_{\infty},il} &= \langle (\widehat{R_{\infty i}} - R_{\infty i})(\widehat{R_{\infty j}} - R_{\infty j}) \rangle \\ &\simeq C_{\infty,il} - C_{\infty,ij} C_{jk}^{-1} C_{\infty,kl}, \end{aligned} \quad (45)$$

The square root of diagonal terms, i.e. $\sqrt{\epsilon_{ii}}$, is the $1\text{-}\sigma$ error bar of MLWE.

The waveform estimators can be used to interpolate or extrapolate the waveform in order to estimate its value when no data is available. This can be done by simply adding a fake observing epoch i_{fake} at the time of interpolation or extrapolation, where the value of data ($R_{i_{fake}}$) should be chosen according to the statistical expectation, i.e. $R_{i_{fake}} = 0$. After introducing such a fake data point, we can apply the MLE as discussed above to interpolate or extrapolate.

4 EXAMPLE

In this section, we use five different examples to show possible applications of the AO algorithm. In all cases, TOAs are generated at three frequencies (400 MHz, 1.4 GHz, and 2.5 GHz), where the parameters for all examples are listed in Table 1. Cases 1-3 are characterized by strong, intermediate and weak signal-to-noise, respectively. Case 4 shows the ability to measure f_L at a much lower frequency than $1/T$ for the DM variation signal. In case 5, we explore the performance of the AO algorithm on the deterministic waveform, where a square waveform is used. Based on the five examples, we also compare the reconstructed DM variation waveform with the results from three other methods: polynomial smoothing (Kaspi et al. 1994; Freire et al. 2012), piecewise linear function fitting (Keith et al. 2013), and point-to-point fitting.

The simulated data can be found in Figure 4 to 8, displayed in the barycentric reference frame. We first simulate the signal components, i.e. the time series of DM variations, red noise, and white noise. Here, the power-law spectral signal is simulated using a large number of independent monochromatic components. The number of compo-

nents (N_{comp}) is taken to be 10^4 in this paper. These components are distributed randomly with a uniform distribution in the logarithmic frequency domain. For each monochromatic component, the amplitudes and phases follow zero-mean Gaussian and 0-to- 2π uniform distributions. The RMS of the amplitudes A of each component is determined via

$$\text{RMS}[A(f)] = 2S(f)f \Delta \ln f \quad (46)$$

where $S(f)$ is the single-side power spectrum that we want to simulate, and $\Delta \ln f$ is the effective bandwidth of the single monochromatic component, which is defined as $\Delta \ln f = (\ln f_{\text{max}} - \ln f_{\text{min}})/N_{\text{comp}}$. f_{max} and f_{min} are the maximal and minimal frequencies that we are concerned with. f_{min} is equal to f_L . The choice of f_{max} is not crucial here, since we are dealing with red noise, for which the high frequency components have little contribution to the signal power. We choose $f_{\text{max}} = 1/\Delta T$, where ΔT is the minimal time difference between two successive observing epochs.

After all of the noise components are computed, we ‘add’ them to the perfect TOA calculated by Tempo 2 (Hobbs et al. 2006). We perform the addition in the barycentric frame. Because of the motion of the Earth, there is a difference between the two methods used to *simulate*, i.e. 1) adding the noise to the barycentric TOA, and 2) adding the noise to the telescope-site TOA. Directly adding the DM-induced delay to the telescope-site TOA is incorrect in principle, because the extra delay due to the Earth’s motion is not accounted for. If one introduces a time shift of Δt in the telescope-site TOA in the simulation, the Earth’s position, when the pulse is arriving, will be mistakenly shifted by $\sim v_e \Delta t$, where v_e is the Earth’s velocity. Depends on the pulsar position, such a wrong position produces a one-year-period residual with an amplitude about $v_e \Delta t/c \simeq 10^{-4} \Delta t$ in the TOAs. For example, if a 1-ms time shift were introduced, a signal with an amplitude of about 100 ns would appear in the residuals. To avoid these complexities, we use the barycentric frame throughout our simulation.

The MCMC method is used to estimate the noise model parameters required to construct the waveform estimators. The detailed descriptions of MCMC methods can be found in many standard references (e.g. Press et al. (2007)). The basic idea of the MCMC is to get a large sample of the noise model parameter sets, of which the distribution obeys the likelihood. The statistical properties of the inferred parameters are directly measured using such samples. We use flat priors in this paper. We have compared the MCMC using the Metropolis-Hastings (Hastings 1970) with affine-invariant ensemble (Goodman & Weare 2010) sampling schemes, but no significant difference was found.

The posterior distributions for the five examples are given in Figure 9 to 13, from which the errors on the noise model parameter estimators are inferred. Our MLEs of the noise parameters are found by applying an optimization step to the MCMC likelihood distribution, where the Nelder–Mead’s downhill simplex method (Jeffrey et al. 1998) is adopted to find the maximum of the likelihood, i.e. equation (31). In this optimization, the initial values are taken to be the set of parameters with maximum value of ρ' among the parameter samples from the MCMC. **There seems to be a small bias within a 2- σ level in estimating f_L . However, the current algorithm is still safe because of following two reasons. On one hand, the**

MCMC posterior distribution already includes such effect in the error estimation. On the other hand, the ensemble statistics of the estimator may not be affected by this apparent bias. The tail in the posterior distribution towards lower f_L naturally makes it infer slightly higher values more frequently while getting lower values on rare occasions.

With the noise model parameters, the waveform of each signal component is reconstructed using equation (36), (37), and (38). Although the covariance matrix C is symmetric, we use the QR decomposition algorithm (Press et al. 2007) instead of the Cholesky decomposition to invert the matrix. This makes the computation slightly slower (still faster than the singular value decomposition implementation), but much more robust. The reconstructed waveforms are also shown in Figure 4 to 8. One can see that the four algorithms generally agree with each other as well as with our injections.

The performances of the four DM reconstruction algorithms can be compared using the standard deviations of the differences between the reconstructed waveforms and the injections. Point-to-point fitting is described in Section 2. The AO waveform estimator is constructed using the parameters found by the MCMC techniques. To apply the polynomial fitting and piecewise linear function methods, one needs the optimal polynomial order and the optimal averaging timescale, respectively. In practical data analysis, the two parameters can be determined through spectral analysis. In practice, estimating those two parameters through spectral analysis can be challenging, and in order not to concern ourselves with the details of such non-related schemes, we use information from the injections. We perform grid searches to find the best parameters that minimize the standard deviations of the differences between the reconstructed waveforms and the injections. **Here, using injections insures that no other parameter search performs better. This helps us determining the best-possible DM variation estimation of the polynomial and piecewise linear function methods for the given data set⁴.** We summarized the results of the comparisons between the methods in Figure 14. One can see that these three methods (polynomial fitting, the piecewise linear function method, and the AO algorithm) produce a comparable level of error, while the AO algorithm generally has a smaller error than the other methods.

The AO algorithm can also be used to recover the deterministic waveforms with sharp jumps as shown in ‘case 5’, although we have assumed a power-law signal model in this paper. In fact, the power-law is the linear approximation of the signal spectrum in log-log space. We expect it to work for most cases, where the dominant part of the spectrum can be approximated by a straight line.

As we have previously explained, the AO algorithm is also capable of extrapolating and interpolating the waveform. The examples are given in Figure 15. For the interpolation problems, polynomial fitting and the MLE give similar results; both are consistent with the simulated injections. For the extrapolation application, the MLE produces much

⁴ It is worth noting that we did not use any injection information for the AO algorithm!

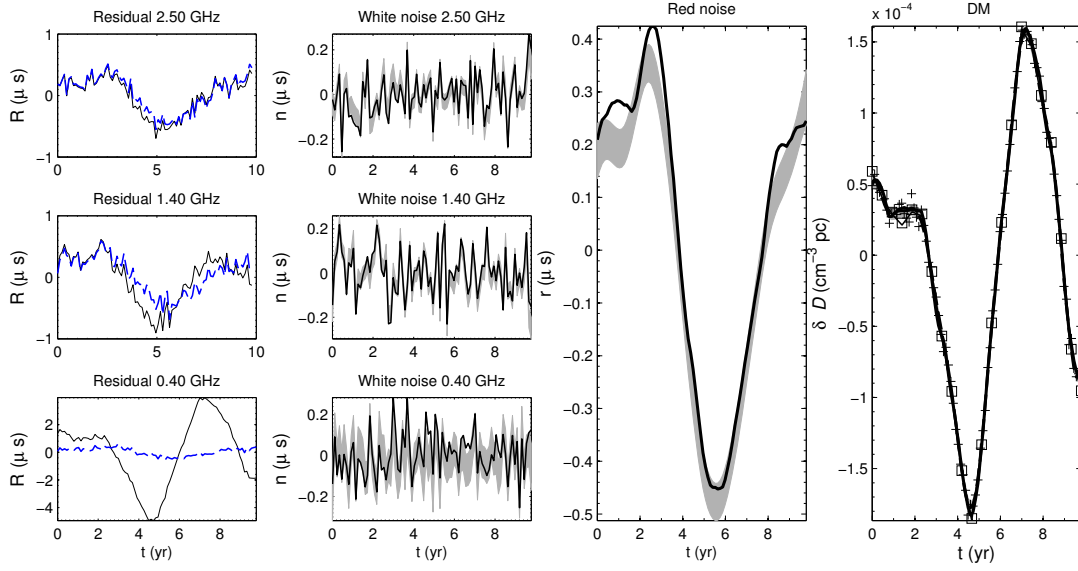


Figure 4. The simulation and waveform reconstruction of ‘case 1’. As shown in the left-most column, the timing residuals are simulated for three frequency bands, i.e. 400 MHz, 1.4 GHz, and 2.5 GHz. The solid lines represent the simulated residuals, while the dashed lines represent the timing residuals after DM variation correction with the AO algorithm. The second column shows the injected white noise waveform at each frequency (solid lines), and the recovered AO waveform (with the grey stripe indicating the error bar). The red noise component is shown in the third column, with the solid line corresponding to the injection, while the gray stripes represent the recovered AO waveform with a $1\text{-}\sigma$ error bar. The DM variation waveform is shown in the fourth column. The solid line, gray stripe, and dashed line represent, respectively, the injection, the AO estimator, and the polynomial fitting waveform. The square symbols are for the piecewise linear function method. The point-to-point fitting results for DM are plotted with the symbol ‘+’. All of the methods produce consistent results. The RMS of the difference between the estimations and injections for all cases and methods are summarized in Figure 14.

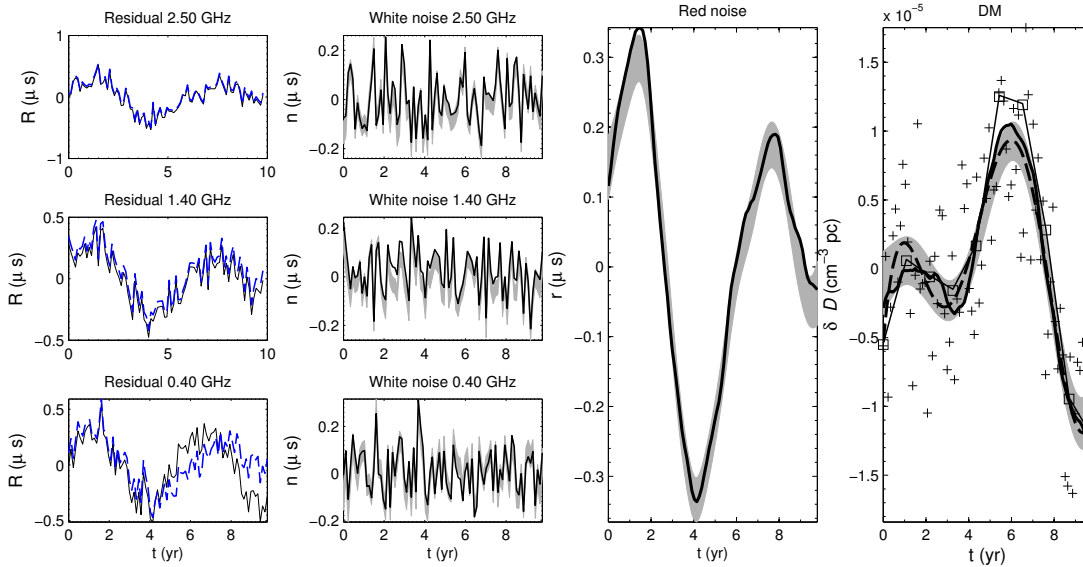


Figure 5. The same as Figure 4 but for ‘case 2’.

more stable results compared to polynomial fitting. Indeed, polynomial fitting quickly diverges from the injections when no observations are available.

5 DISCUSSION AND CONCLUSION

In this paper, we have constructed an algorithm to estimate the waveform of DM variations and infinite-frequency TOAs from multi-frequency datasets. This algorithm is based on the MLE, which makes the presented algorithm AO, i.e. it approaches the Cram r-Rao bounds as the signal-to-noise ratio becomes high (Chen 2009). We demonstrated the appli-

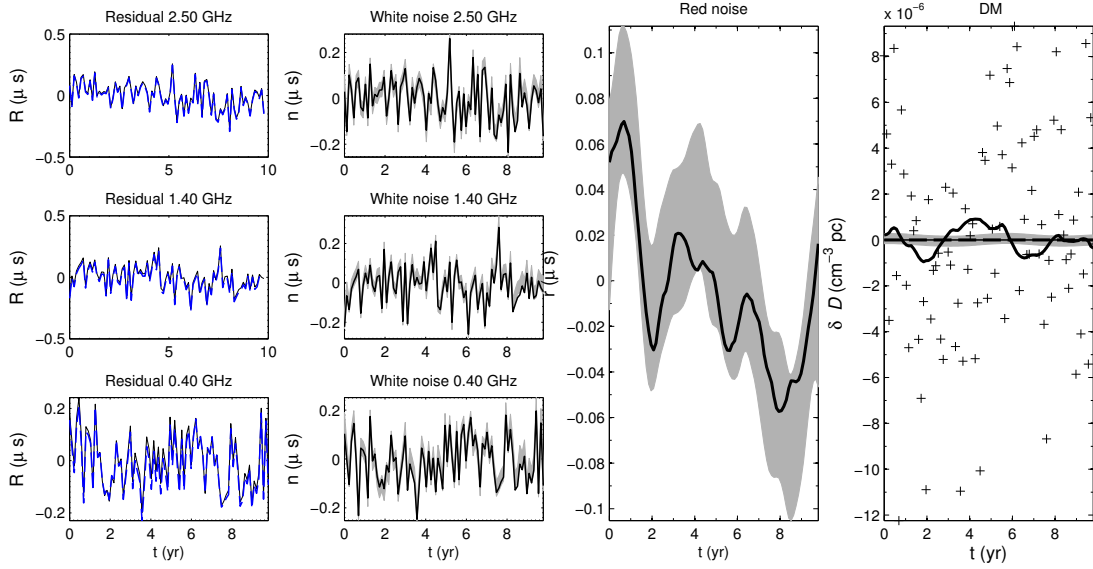


Figure 6. The same as Figure 4 but for ‘case 3’.

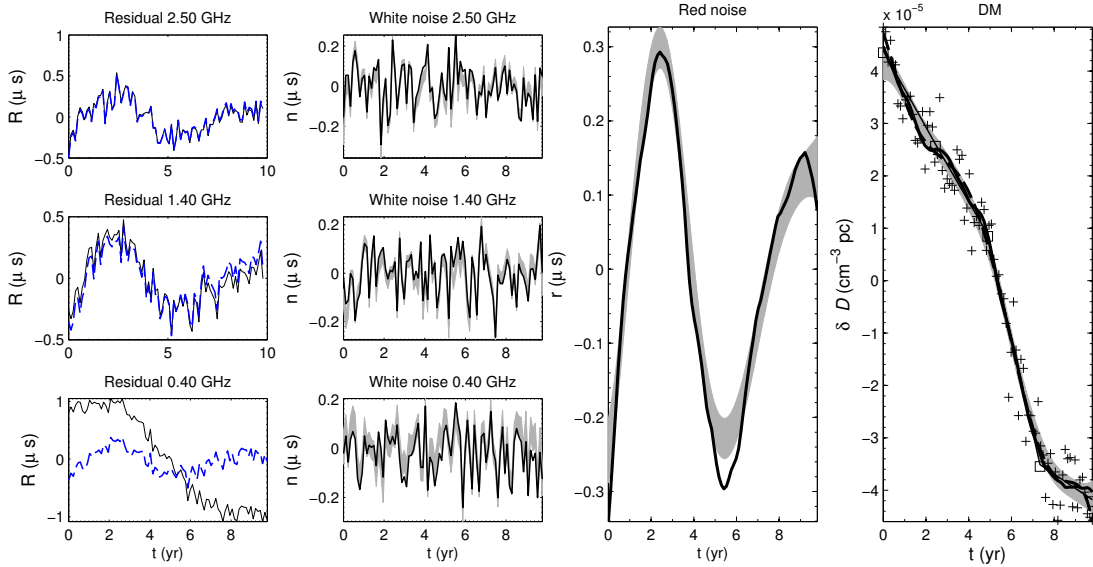


Figure 7. The same as Figure 4 but for ‘case 4’.

cation of the algorithm on a simulated data set at 400 MHz, 1.4 GHz, and 2.5 GHz with DM variations and red timing noise included. Parameter estimates were found with a likelihood analysis, carried out using an MCMC algorithm. The maximum likelihood parameter inferences were subsequently found using the downhill-simplex algorithm, which in turn was used to produce waveform estimators and a reconstruction of all components of the injected signal. One can see from Figure 4 to Figure 13 that the noise model parameters and the waveform estimator both produce results that are consistent with the injections.

Our current method resolves the structures at smaller time scales better than the polynomial and piecewise linear function methods, as shown in Figure 4 to 8. This is due to the properties of equation (36), (37), and (38). We can in-

terpret the correlation matrix C as the ‘power of signal’, i.e. the second order statistics of the waveform. The mechanism of the filter can thus be understood as the weighted average of inputs, i.e. in terms of Feynman’s illustration notation

$$\text{Estimated signal } [\mathbf{r}] = \frac{\text{power of the signal } [\mathbf{C}_r]}{\text{power of all signals } [\mathbf{C}]} \times \text{all signals } [\mathbf{s}].$$

In this way, as long as the power of the signal under investigation is higher than the power of the rest of the components, one will be able to accurately estimate its waveform on the relevant time scales. In the case of polynomial interpolation, such small-scale resolutions are limited due to polynomial order and numerical instability.

We have included the low frequency cut-off of DM variations as one of the model parameters. **Such low frequency cut-off, if measured, may shed light on the driven**

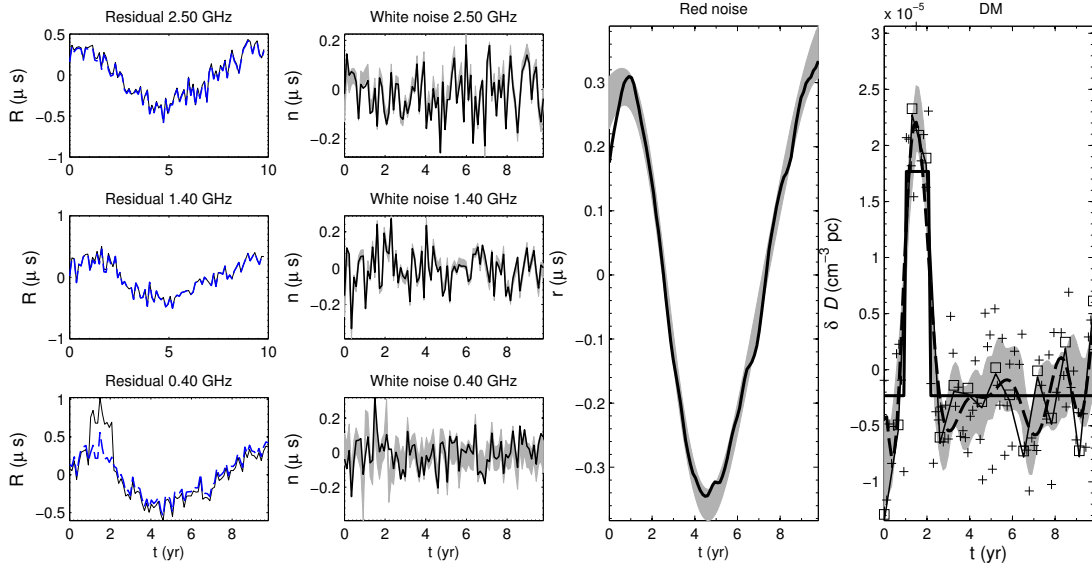


Figure 8. The same as Figure 4 but for ‘case 5’.

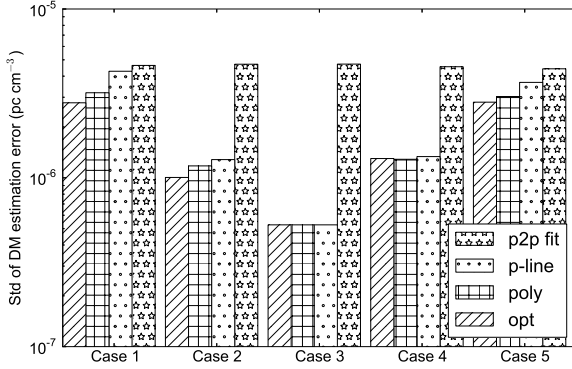


Figure 14. The standard deviations of the difference between the reconstructed waveforms and injections of DM variations for all five cases. In the legend, ‘opt’, ‘poly’, ‘p-line’, and ‘p2p’ denote the AO algorithm, polynomial smoothing, the piecewise linear function, and point-to-point fitting, respectively. We can see that the AO algorithm, polynomial fitting and the piecewise linear function method have similar performance, and that all perform better than point-to-point fitting. The AO algorithm slightly outperforms other methods for most of the cases in this paper.

mechanism of interstellar medium turbulence. On the other hand, similarly to using the period and period derivative of pulsar timing parameters, we can use time derivatives of DM to regularize the signal (for a good example, see Lentati et al. 2013). Either of the methods can be used to construct the optimal filter for the mitigation of DM variations. For the application of extrapolation however, using such a polynomial regularization may impair long-term stability.

In this paper, both the MLEs of the noise model parameters and of the waveforms are purely time-domain operations. This method therefore does not require uniform sampling of the data nor synchronization of the observing session, i.e. it does not require the data to be taken on a regular basis nor to be perfectly aligned in time. Further-

more, this method does not need to interpolate the signal. This makes it particularly suitable for pulsar timing problems, where the data are usually non-uniformly distributed and the multi-frequency observations are not simultaneous. As shown in Figure 15, this method can be used to interpolate or extrapolate the estimation of DM variations to epochs where no observations are available. We can see that interpolation using this method is comparable to polynomial fitting, while its performance is much better when extrapolating DM variations.

We have also investigated DM variations and infinite frequency TOA measurement accuracy for single observing epochs analytically. From equation (9) and (10), we can see that it is important to have good frequency coverage to mitigate the effects of DM variations. The larger the frequency range, the better accuracy we can achieve for measuring \mathcal{D} and T_∞ . From equation (9), the RMS error of T_∞ is the weighted sum of the noise level of individual frequencies with a weighting factor of ν^4 . In this way, higher frequency data will have a higher weight in determining T_∞ . Additionally, we have shown in Section 2 that increasing the accuracy of high frequency data is important for breaking the degeneracy between \mathcal{D} and T_∞ . Because of the steep flux spectral index of pulsars, obtaining better precision in high frequency data is a challenge. This fact should be included in the efforts to optimize pulsar timing array schedules (e.g. Lee et al. 2012). The weighting factors for DM accuracy (equation (10)) are the same for both frequencies. Therefore, the low frequency data from future telescopes with a larger collecting area will become very useful for measuring DM variations. We also expect that the Five-hundred-meter Aperture Spherical Radio Telescope (FAST, Nan et al. 2006; Smits et al. 2009) and the Square Kilometre Array (SKA, Kramer & Stappers 2010; Smits et al. 2009) will provide unique opportunities to study DM variations and interstellar electron density fluctuations.

The MLE described here is also applicable to many other pulsar timing related problems. For example, the same

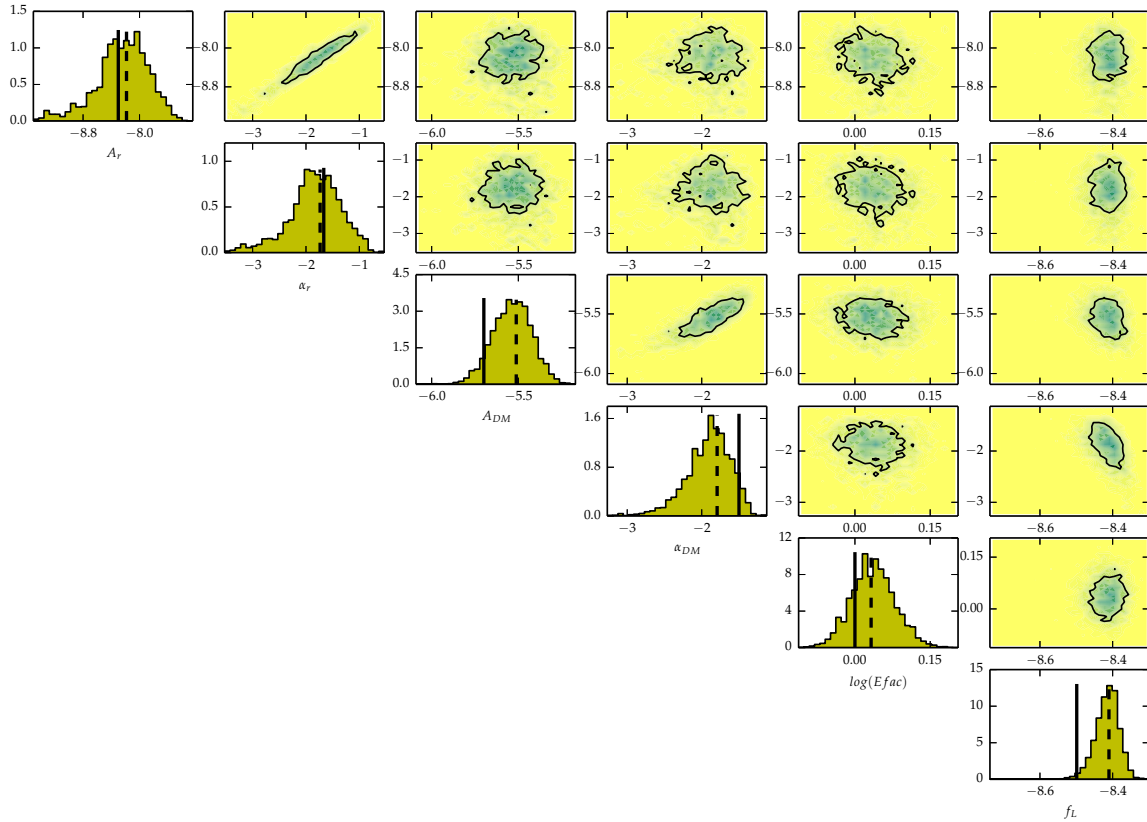


Figure 9. The marginalized posterior distribution of the estimated model parameters using MCMC. The contour and curve plots in this figure represent the 2-D and 1-D marginalized posterior distributions. The density of gray in the contour plots indicates the confidence level, while the solid contours are the 1-sigma confidence levels. The corresponding parameters of the 1-D marginalized posterior distributions are indicated on the x-axis. The solid and dashed vertical lines indicate the injected and the maximal-likelihood parameters. We can see that the parameter estimations generally agree with the injections. Since the posterior distributions are usually not perfectly Gaussian, the χ^2 -type parameter fitting may generate biases in parameter estimating procedures.

framework can be used to measure the gravitational wave waveform or to build a pulsar time scale for pulsar timing arrays. The statistical properties (i.e. spectral indices and amplitudes) and waveforms of gravitational waves are estimated simultaneously. This will provide the most complete description of the related processes. As we have shown, by extrapolation, the current method can be used as a predictor to estimate the waveform of the signal at the epoch where no data is yet available. This is critical for the pulsar time scale and pulsar navigation problems (Deng et al. 2013), where one needs an estimation of the quantities (e.g. time defined by pulsar rotation) *now*. On the other hand, for the problem of gravitational wave detection, DM variations can be included in the likelihood, however it is not necessary to estimate the waveform. As such, one can marginalize over the DM variation model parameters after sampling, and focus solely on gravitational wave detection.

As a caveat, the ‘AO’ algorithm is model-based, where we have assumed: 1) a cold free electron model for DM, i.e. DM-induced delays that scale with ν^{-2} , 2) the noise spectra are power-law. Armstrong et al. (1995) had shown

that a power-law spectrum holds for a rather wide range of frequencies. Recently, Lentati et al. (2013) showed that the DM variations of certain pulsars agree with a power-law modeling. From recent structure function measurements of DM variations (Keith et al. 2013), it was shown that most of Parkes Pulsar Timing Array pulsars follow power laws, although the spectral indices deviate significantly from that of a Kolmogorov spectrum. However, it is possible that the two assumptions could be violated in certain cases. **For example, the variation of scattering may introduce a frequency dependent delay that causes deviations from a ν^{-2} law (Hemberger & Stinebring 2008). This may have been observed for some millisecond pulsars already (Keith et al. 2013).**

Investigating the systematics with real data is important for justifying the assumptions made. We anticipate that future high precision timing data from pulsar timing array experiments will help us better understand the noise models. Once a better model for DM variations becomes available, we can include the modeling in the current MLE framework in a straightforward manner. In other words, future high

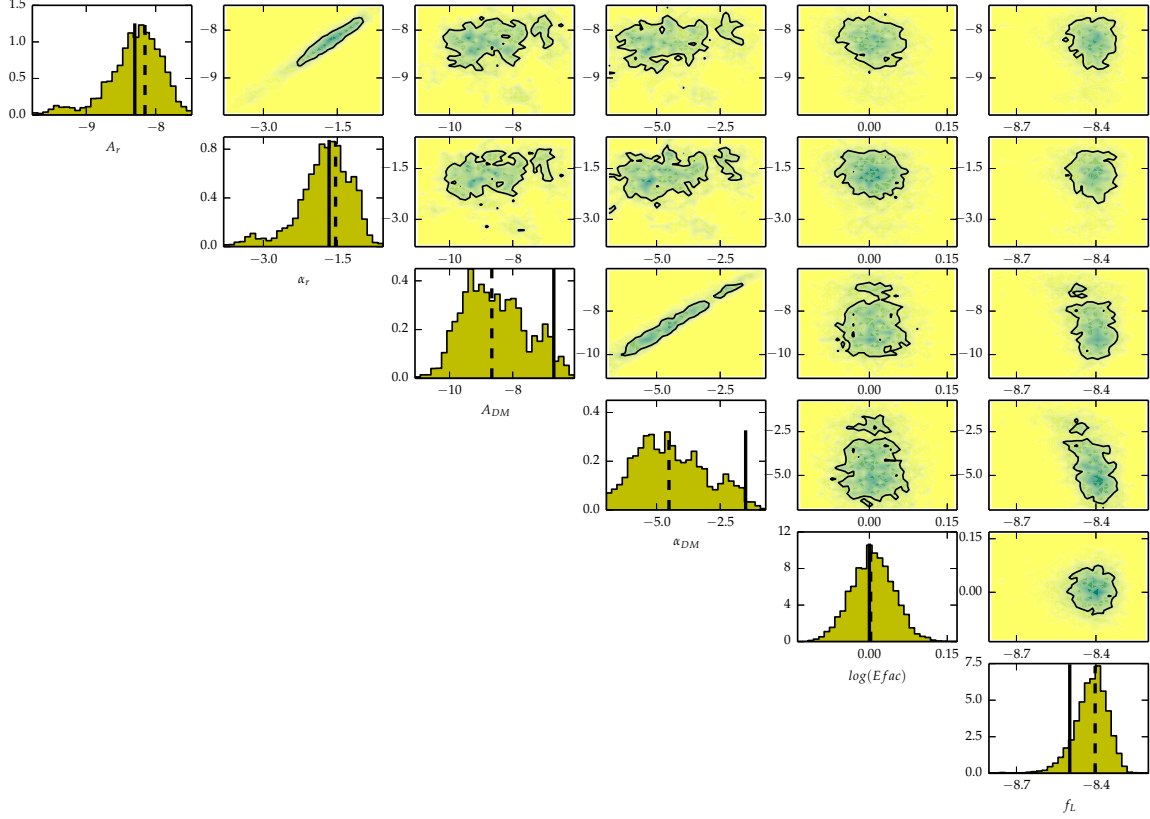


Figure 10. The same as Figure 9 but for ‘case 2’.

precision timing data not only helps us justify the assumptions made, but will also help us improve the AO algorithm itself.

6 ACKNOWLEDGEMENT

K. J. Lee gratefully acknowledges support from the ERC Advanced Grant “LEAP”, Grant Agreement Number 227947 (PI Michael Kramer) and from the National Natural Science Foundation of China (Grant No.11373011). We thank Dan Stinebring for helpful discussions. R.vH. is supported by NASA Einstein Fellowship grant PF3-140116.

APPENDIX A: COVARIANCE MATRIX OF ESTIMATOR

The covariance matrix of the waveform estimator is given by

$$\begin{aligned}
 \epsilon_{r,ij} &= \langle (\hat{r}_i - r_i)(\hat{r}_j - r_j) \rangle \\
 &= \langle (\hat{\mathbf{C}}_r \hat{\mathbf{C}}^{-1} \mathbf{R} - \mathbf{r})(\hat{\mathbf{C}}_r \hat{\mathbf{C}}^{-1} \mathbf{R} - \mathbf{r})^T \rangle \\
 &\simeq \mathbf{C}_r \mathbf{C}^{-1} \mathbf{C}_r - \mathbf{C}_r \mathbf{C}^{-1} \mathbf{C}_r - \mathbf{C}_r \mathbf{C}^{-1} \mathbf{C}_r + \mathbf{C}_r \\
 &= \mathbf{C}_r - \mathbf{C}_r \mathbf{C}^{-1} \mathbf{C}_r, \tag{A1}
 \end{aligned}$$

where we neglect the small correlation between the estimation of the covariance matrix \mathbf{C} and the signal \mathbf{R}, \mathbf{r} .

REFERENCES

- Armstrong J. W., 1984, *Nature*, 307, 527
 Armstrong J. W., Rickett B. J., Spangler S. R., 1995, *ApJ*, 443, 209
 Backer D. C., Hama S., van Hook S., Foster R. S., 1993, *ApJ*, 404, 636
 Champion D. J., et al., 2010, *ApJL*, 720, L201
 Chen X., 2009, *Advanced mathematical statistics*, “Gao Deng Shu Li Tong Ji Xue”, in Chinese, Publisher of University of Science and Technology of China, Hefei, China, 2009
 Coles W., Hobbs G., Champion D. J., Manchester R. N., Verbiest J. P. W., 2011, *MNRAS*, 418, 561
 Cordes J. M., Shannon R. M., 2010, *ArXiv e-prints*
 Cordes J. M., Stinebring D. R., 1984, *ApJL*, 277, L53
 Cordes J. M., Wolszczan A., Dewey R. J., Blaskiewicz M., Stinebring D. R., 1990, *Apj*, 349, 245
 Deng X. P., Coles W., Hobbs G., Keith M. J., Manchester R. N., Shannon R. M., Zheng J. H., 2012, *MNRAS*, 424, 244
 Deng X. P., Hobbs G., You X. P., Li M. T., Keith M. J., Shannon R. M., Coles W., Manchester R. N., Zheng J. H.,

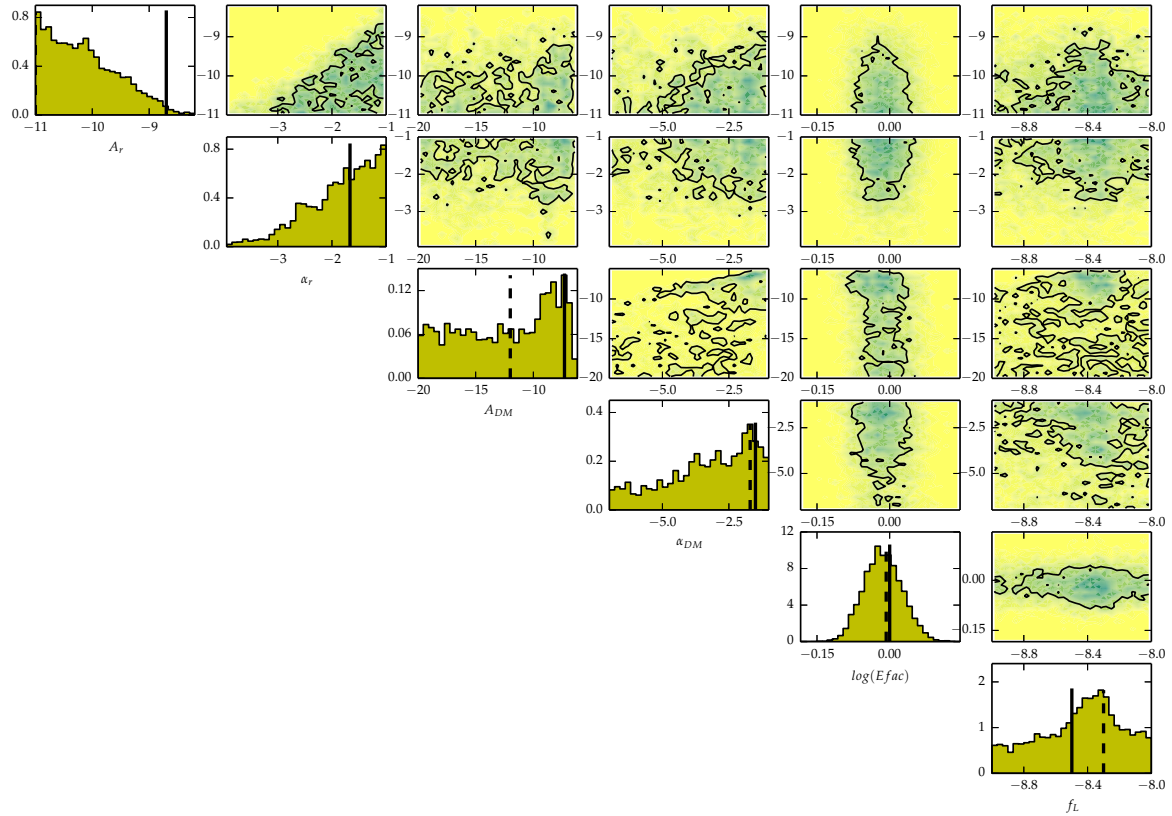


Figure 11. The same as Figure 9 but for ‘case 3’.

Yu X. Z., Gao D., Wu X., Chen D., 2013, *Advances in Space Research*, 52, 1602
 Dodge Y., 2006, *The Oxford Dictionary of Statistical Terms*. Oxford: Oxford University Press
 Edwards R. T., Hobbs G. B., Manchester R. N., 2006, *MNRAS*, 372, 1549
 Enßlin T. A., Frommert M., 2011, *Phy. Rev. D*, 83, 105014
 Foster R. S., Backer D. C., 1990, *ApJ*, 361, 300
 Freire P. C. C., et al., 2012, *MNRAS*, 423, 3328
 Goodman J., Weare J., 2010, *Communications in Applied Mathematics and Computational Science*, 5
 Hastings W. K., 1970, *Biometrika*, 57
 Hemberger D. A., Stinebring D. R., 2008, *ApJL*, 674, L37
 Hobbs G., et al., 2012, *MNRAS*, 427, 2780
 Hobbs G. B., Edwards R. T., Manchester R. N., 2006, *MNRAS*, 369, 655
 Hotan A. W., van Straten W., Manchester R. N., 2004, *PASA*, 21, 302
 Isaacman R., Rankin J. M., 1977, *ApJ*, 214, 214
 Ishimaru A., 1978, *Wave propagation and scattering in random media*. Vol.1., by Ishimaru, A.. New York (NY, USA): Academic Press, 270 p.
 Jeffrey C. L., James A. R., Margaret H. W., Paul E. W., 1998, *SIAM Journal of Optimization*, 9, 112
 Jenet F. A., Armstrong J. W., Tinto M., 2011, *Phys. Rev.*

D, 83, 081301
 Jenet F. A., Hobbs G. B., Lee K. J., Manchester R. N., 2005, *ApJL*, 625, L123
 Kariya T., Kuruta H., 2004, *Generalized Least Squares*, John Wiley & Sons, NJ, USA, 2004
 Kaspi V. M., Taylor J. H., Ryba M. F., 1994, *ApJ*, 428, 713
 Keith M. J., et al., 2013, *MNRAS*, 429, 2161
 Kramer M., Stappers B., 2010, in *ISKAF2010 Science Meeting - ISKAF2010*, June 10-14, 2010 Assen, the Netherlands LOFAR, LEAP and beyond: Using next generation telescopes for pulsar astrophysics . p. 10
 Landau L. D., Lifshitz E. M., 1960, *Electrodynamics of continuous media*, Pergamon Press, Oxford, Egnland, 1960
 Lee K. J., Bassa C. G., Janssen G. H., Karuppusamy R., Kramer M., Smits R., Stappers B. W., 2012, *MNRAS*, 423, 2642
 Lee Y. W., 1967, *Statistical Theory of Communication*. New York: John Wiley & Sons
 Lentati L., Alexander P., Hobson M. P., Feroz F., van Haasteren R., Lee K., Shannon M., 2013, submitted
 Liu K., et al., 2013, in preparing
 Liu K., Keane E. F., Lee K. J., Kramer M., Cordes J. M., Purver M. B., 2012, *MNRAS*, 420, 361
 Lommen A. N., 2012, *Journal of Physics Conference Series*,

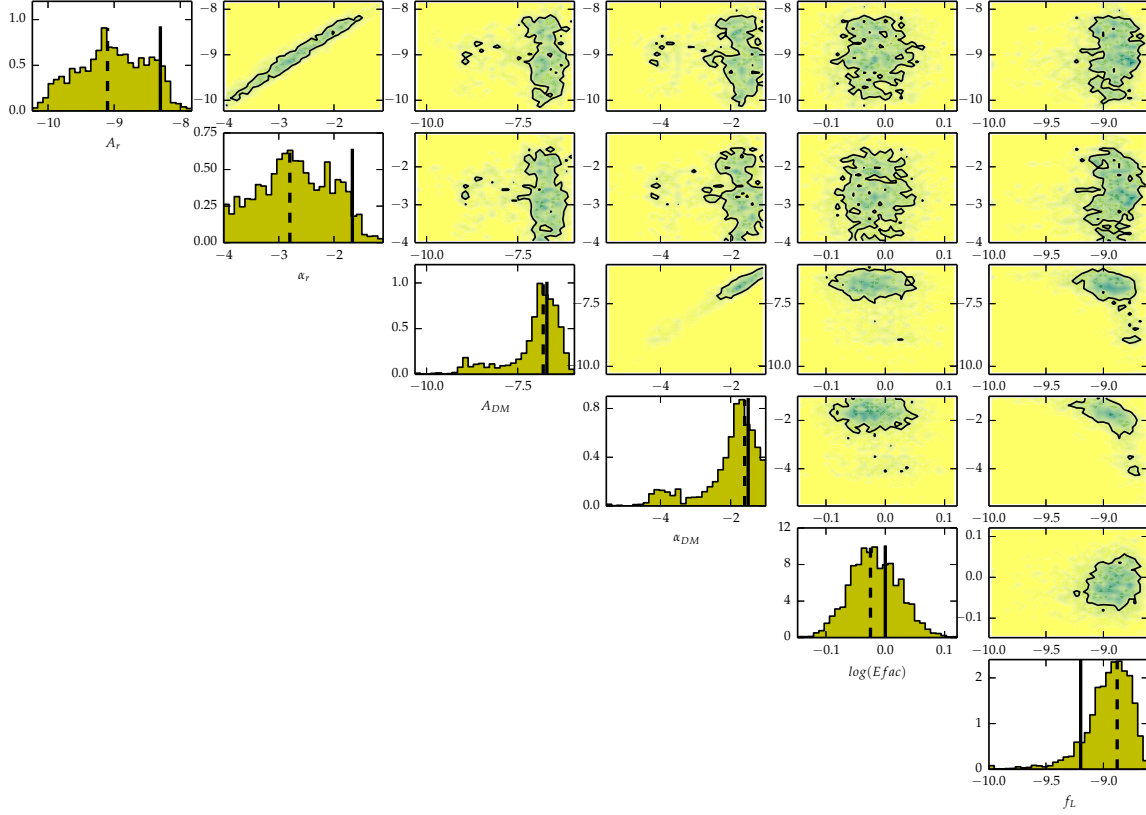


Figure 12. The same as Figure 9 but for ‘case 4’.

363, 012029

Nan R., Wang Q., Zhu L., Zhu W., Jin C., Gan H., 2006, Chinese Journal of Astronomy and Astrophysics Supplement, 6, 020000

Petroff E., Keith M. J., Johnston S., van Straten W., Shannon R. M., 2013, MNRAS, 435, 1610

Phillips J. A., Wolszczan A., 1991, ApJL, 382, L27

Press W. H., Teukolsky S., Vetterling W. T., Flannery B. P., 2007, Numerical recipes: the art of scientific computing. Cambridge University Press, Cambridge, UK

Ramachandran R., Demorest P., Backer D. C., Cognard I., Lommen A., 2006, ApJ, 645, 303

Rankin J. M., Counselman III C. C., 1973, ApJ, 181, 875

Rankin J. M., Roberts J. A., 1971, in Davies R. D., Graham-Smith F., eds, The Crab Nebula Vol. 46 of IAU Symposium, Time Variability of the Dispersion of the Crab Nebula Pulsar. p. 114

Smits R., Kramer M., Stappers B., Lorimer D. R., Cordes J., Faulkner A., 2009, A&A, 493, 1161

Smits R., Lorimer D. R., Kramer M., Manchester R., Stappers B., Jin C. J., Nan R. D., Li D., 2009, A&A, 505, 919

van Haasteren R., Levin Y., 2013, MNRAS, 428, 1147

van Haasteren R., Levin Y., McDonald P., Lu T., 2009, MNRAS, 395, 1005

Wu X., Chian A. C.-L., 1995, ApJ, 443, 261

You X. P., et al., 2007, MNRAS, 378, 493

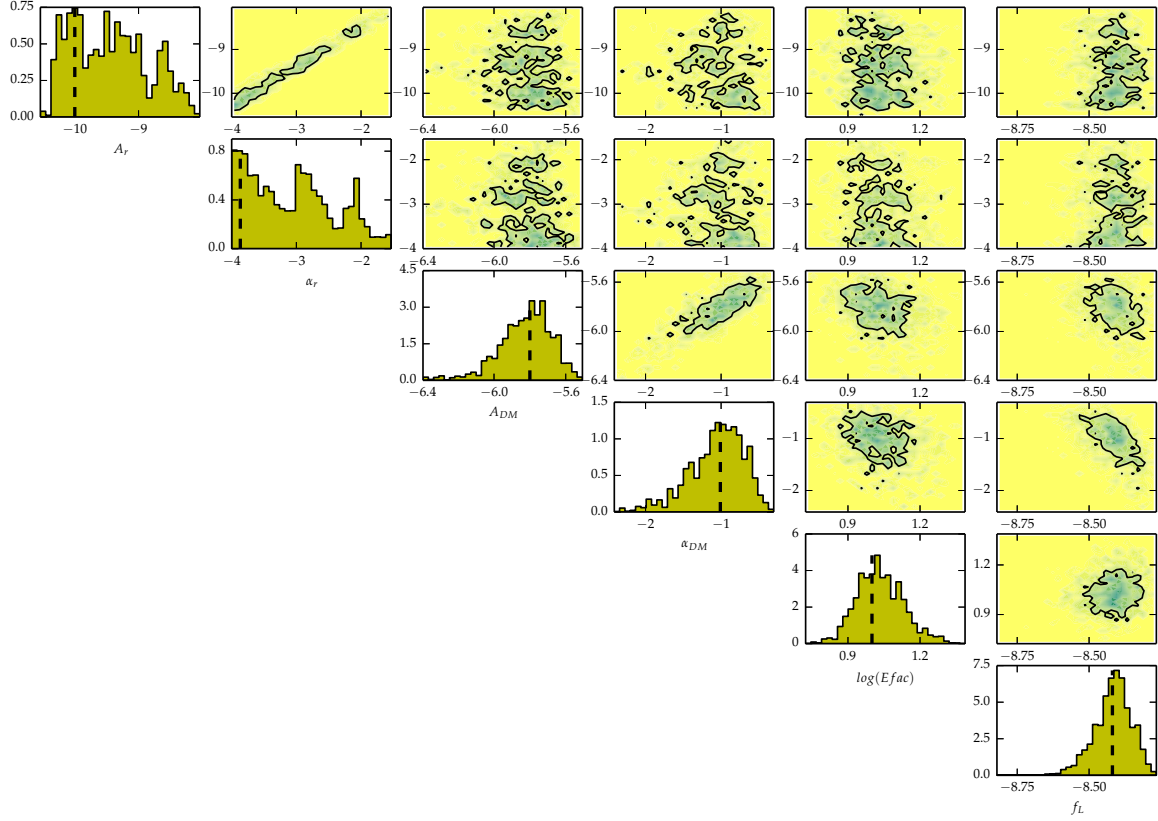


Figure 13. The same as Figure 9 but for ‘case 5’.

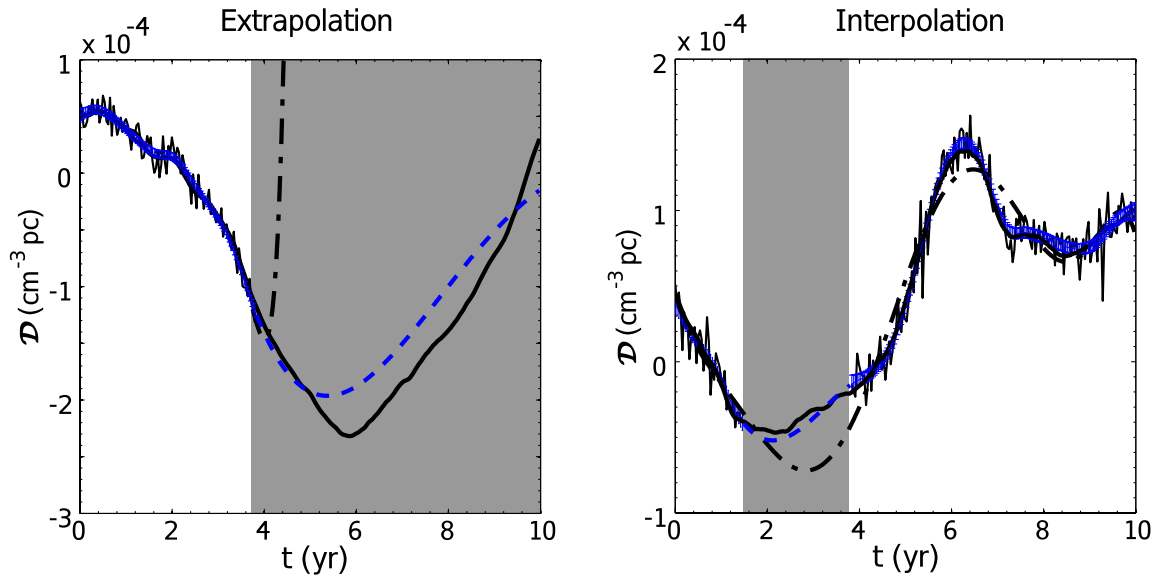


Figure 15. Extrapolation and interpolation using the MLE. The left and right panels show the results of DM variation extrapolation and interpolation, respectively. The solid curves represent the simulated DM variation injections, while the dashed curves with error bars represent the results of the AO algorithm. The thin black curve represents point-to-point fitting, while the dash-dotted curve represents polynomial interpolation estimates. In the waveform estimation process, the data points in the gray shaded region are removed to simulate the effects of extrapolation and interpolation. The point-to-point fitting algorithm gives no prediction in the gray shaded region.